TRACKING OF WAVEFRONTS

J. Bahrdt, BESSY, Berlin, Germany

Abstract

The design of beamlines for VUV and X-ray FEL facilities requires a detailed knowledge of the coherent radiation source. Time dependent simulations with FEL codes like GENESIS provide the electric field distribution at the end of the FEL which represents the complete information. Ray tracing codes used to transform the light from the source to the sample are generally based on geometrical optics and do not include directly the coherent properties of the FEL radiation. On the other hand Fourier optic techniques are usually applied to the propagation across normal incidence optics. We present an algorithm based on physical optics which permits the propagation of wavefronts across grazing incidence optics including interference effects, diffraction, polarization variation and pulse lengthening. Examples are given for the proposed BESSY Soft X-Ray FEL and a 3rd generation storage ring beamline.

INTRODUCTION

The next generation of synchrotron radiation facilities is based on FEL sources. The radiation properties are superior to those of storage rings in many aspects. The peak brightness overcomes the numbers of third generation machines by 10 orders of magnitude; the pulse length is in the fs-regime; the light is transversely coherent (SASE [1], [2], [3] and HGHG [4]) and longitudinally coherent (HGHG).

The photon beam quality depends strongly on the parameters of the electron gun, the linac and the FEL undulators. Extensive start-to-end simulations have been performed at various laboratories to estimate the radiation properties at the end of the last undulator module including tolerances.

Table 1: Comparison of geometrical and physical optic codes.

	geometrical optic	physical optic
total intensity	yes	yes
brightness	yes	yes
field amplitudes	no	yes
diffraction limited source	no	yes
diffraction effects of beamline	indirect	yes
polarization modulation in beamline	no	yes
time structure	indirect	yes

The user of an FEL facility will be interested in the beam quality at the experiment. Consequently, the start-to-end simulations have to be extended to include also the beamline. Ray tracing codes used in the past are generally based on geometrical optics. These codes can not simulate directly the important coherent properties of the FEL radiation.

In this paper we will present the physical optics code PHASE which has been written over the last years at BESSY. Table 1 shows the advantages of physical optics codes with respect to geometrical optics codes.

In the next section the propagation of radiation in normal incidence geometries is described. Then, a matrix formalism is presented which permits the propagation through grazing incidence optics. The simulation of the time dependence which has recently been added to the code will be explained in more detail. Next, a few details to the code PHASE are discussed and finally, examples for various aspects of the radiation propagation are presented.

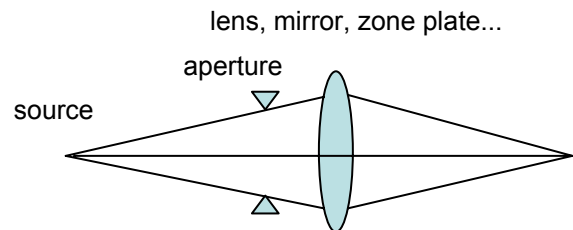## FREE SPACE PROPAGATION AND NORMAL INCIDENCE OPTICS

Figure 1: Principle layout of a normal incidence optic.

For monochromatic waves the electric field distribution in a plane perpendicular to the direction of propagation completely defines the properties of the radiation (Huygens' construction). The wavefront can be propagated by a direct integration of the equation of Fresnel and Kirchhof (eq.1) which is, however, time comsuming.

$$\vec{E}(z', y') = \frac{1}{\lambda} \int\limits_{-\infty}^{\infty}\int\limits_{-\infty}^{\infty} \vec{E}(z, y) \frac{e^{i\vec{k}(\vec{r}-\vec{r}')}}{|\vec{r} - \vec{r}'|} \cos(\beta) \cdot dy \cdot dz$$

(1)

Alternatively, in Fourier optics [5] the original field distribution is Fourier transformed to obtain plane waves with different angles. The drift Δx is applied by multiplication of an appropriate phase factor. A Fourier back transformation yields the field distribution at the new location (eq.2-4).

$$\vec{E}_0(\nu_z, \nu_y) = \int\limits_{-\infty}^{\infty}\int\limits_{-\infty}^{\infty} \vec{E}(z, y) \cdot e^{-2\pi i(\nu_z z + \nu_y y)} dy \cdot dz$$

(2)

$$\vec{E}(v_z, v_y) = \vec{E}_0(v_z, v_y) \cdot e^{2\pi i \cdot \Delta x \cdot \sqrt{1/\lambda^2 - v_z^2 - v_y^2}} \quad (3)$$

$$\vec{E}(z', y') = \int_{-\infty}^{\infty} \int_{-\infty}^{\infty} \vec{E}(v_z, v_y) \cdot e^{2\pi i \cdot (v_z z + v_y y)} \cdot dv_y \cdot dv_z \quad (4)$$

Normal incidence optical elements (lens, zone plate, aperture etc.) are introduced by multiplication of an appropriate complex matrix in real space.

The fractional frequency bandwidth of the new soft X-ray and X-ray FELs is typically a few 0.001. To take this into account the simulations have to be performed for various frequencies. The time dependent FEL code GENESIS [6] provides the complex electric field vectors on a transverse grid. In the time dependent mode a large number of slices represents the time evolution of the electric fields at each grid point. Before starting the wavefront propagation the time dependent electric fields E(t) have to be converted to frequency dependent variables (E(ω)) via a Fourier transformation for each individual grid point. Equations 2-4 are applied successively to the transverse field distributions of each frequency and finally, the result is back transformed to time space.

GENESIS evaluates photon beam properties at the end of the FEL where the radiation is already divergent. Following the described procedure these data can be propagated in order to derive information on the effective location of the photon beam waist and the size of the phase space [7].
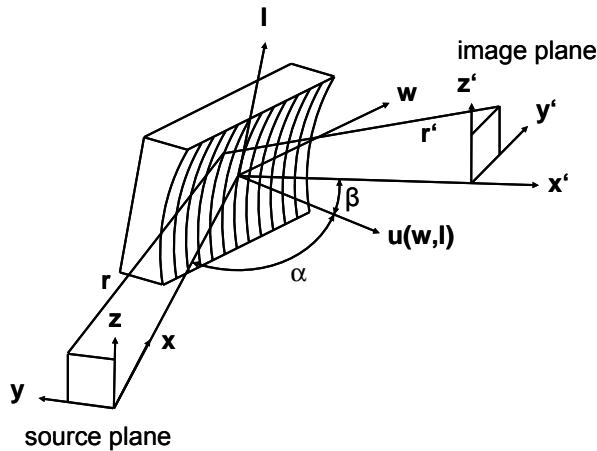
GRAZING INCIDENCE OPTICS

Figure 2: Coordinate system and definition of variables.

In this section we will briefly describe the formalism of the physical optics code PHASE. For detailed information we refer to [8], [9]

The propagation of an electric field distribution is given by eq. 5 using the propagator h where b is the transmittance of the optical element.

$$\vec{E}(\vec{a}') = \int h(\vec{a}', \vec{a}) \cdot \vec{E}(\vec{a}) \cdot d\vec{a} \quad (5)$$

$$h(\vec{a}', \vec{a}) = \frac{1}{\lambda^2} \int_{Surface} \frac{\exp(ik(r+r'))}{rr'} \cdot b(w, l) \cdot \cos(\alpha) \cdot dw \cdot dl$$

The integration is performed over the complete surface of the optical element. For a combination of several optical elements it is advantageous to substitute the source coordinates ($\vec{a} = (z, y)$) with the divergencies in the image plane (eq.6).

$$\vec{E}(\vec{a}') = \int h(\vec{a}', \vec{a}) \cdot \vec{E}(\vec{a}) \cdot \left| \frac{\partial(y, z)}{\partial(dy', dz')} \right| \cdot d(dy') \cdot d(dz') \quad (6)$$

The propagator for two optical elements is given by an integral over the product of two individual propagators of the two elements (eq.7).

$$h(\vec{a}'', \vec{a}) = \int h_2(\vec{a}'', \vec{a}') \cdot h_1(\vec{a}', \vec{a}) \cdot d\vec{a}' \quad (7)$$

The number of dimensions for integration increases with the number of elements and an approximation is required to restrict the computation time to reasonable values. For typical grazing incidence optics at synchrotron radiation light sources the propagator of one optical element can be simplified applying the stationary phase approximation [10]. The principle of this approximation is the following: i) the asymptotic behavior ($k \rightarrow \infty$) of the integral of the propagator h in eq.5 is completely defined by the behavior of the integrand at the critical points. The critical points of the first kind are locations where the first derivatives of $r + r'$ with respect to w and l are zero (the second derivatives are non zero) and the critical points of the second kind are the points on the boundary, where the derivative of $r + r'$ along the boundary is zero. ii) the leading term in the asymptotic expansion is the contribution from the critical points of the first kind, if there are any. This term for one critical point is shown in eq.8, where the distances r_0 and r_0' refer to the paths lengths to the critical point. The integrals can be solved analytically if the integration limits are set to infinity.

$$h(\vec{a}, \vec{a}') \approx const \cdot \frac{1}{r_0 r'_0} \exp[ik(r_0 + r'_0)] \cdot$$
$$\int \exp[ik(w^2/c_1^2)] \cdot dw \cdot \int \exp[ik(l^2/c_2^2) \cdot dl \quad (8)$$

The expressions c_1 and c_2 contain the derivatives of the optical path length p with respect to the surface coordinates w and l at the critical points. With this simplification eq.5 reduces to eq.9. The dimensions of integration have been reduced from 4 to 2.

$$\vec{E}(\vec{a'}) = const \cdot \int \vec{E}(\vec{a}) \cdot \frac{\exp[ik(r_0 + r_0')]}{r_0 r_0'} \cdot$$

$$\left| \frac{\partial^2 p}{\partial w^2} \cdot \frac{\partial^2 p}{\partial l^2} - \left(\frac{\partial^2 p}{\partial w \cdot \partial l} \right)^2 \right|^{-0.5} \cdot \left| \frac{\partial(y, z)}{\partial(dy', dz')} \right| \cdot d(dy') \cdot d(dz')$$

$$(9)$$

We assume that for most of the relevant geometries the critical points of the first kind are well separated (figure 3). Then, the leading term of the expansion described by eq.8 is sufficient. This term has been implemented into PHASE. If necessary, higher order terms will be implemented in the future as well.
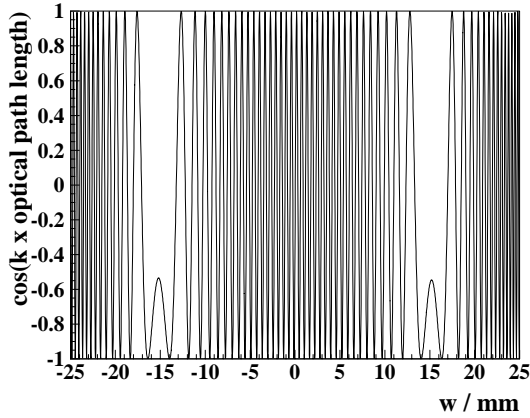

Figure 3: Cosine of the optical path versus the optical element coordinate w for a demagnifying mirror. The fast oscillating amplitudes do not contribute to the integral.

In [10] an analytic expression for the leading term of the contributions from the critical points of the second kind is given. This expression is, however, not implemented into PHASE because it is assumed that in most cases the optical elements do not scrape the photon beam. In cases where this assumption is not true the propagation has to be split into two steps where the beam is propagated from the source to an aperture in front of the limiting element and then, propagated to the image plane.

Replacing the surface coordinates (w, l) in the optical path with coordinates of the source and the image plane (eq.10) we get the equation of propagation across one element.

$$\left| \frac{\partial^2 p}{\partial w^2} \cdot \frac{\partial^2 p}{\partial l^2} - \left(\frac{\partial^2 p}{\partial w \cdot \partial l} \right)^2 \right|^{-0.5} \cdot \frac{\cos(\alpha)}{r_0 r_0'} \Rightarrow \left| \frac{\partial(y', z')}{\partial(dy, dz)} \right|^{-0.5} \quad (10)$$

Based on these expressions a fourth order transformation map between the image coordinates (y_f, z_f, dy_f, dz_f) and the source coordinates (y_i, z_i, dy_i, dz_i) is generated. Using the expansion coefficients a 70x70 transformation matrix for the transformation of all coordinates and angles as well as all cross products is

established. The generally nonlinear transformation of the coordinates and angles can now be expressed by a linear operation (eq.11).

$$\overline{Y}_f = \overline{\overline{M}} \cdot \overline{Y}_i$$

$$\overline{Y}_f = (y_f, z_f, dy_f, dz_f, y_f^2, y_f z_f ...) \quad (11)$$

The transformation across several optical elements is simply described by the product matrix of all individual matrices (eq.12).

$$\overline{Y_N} = \left(\prod_{k=m+1}^{N} \overline{\overline{M_k}} \right) \cdot \overline{Y_m} \quad (12)$$

POLARIZATION ANALYSIS

The polarization properties of the final field distribution is analyzed via a projection of the field vectors onto the projection vectors $\vec{S}$ (see eq.13). The resulting intensities can then be converted to the well known Stokes parameters.

$$I_r = \left| \vec{E} \cdot \vec{S}_r^* \right|^2 = \frac{1}{2} \left| E_z - iE_y \right|^2 \quad (13)$$

$$\vec{S}_h = [(1,0)]$$
$$\vec{S}_v = [(0,1)]$$
$$\vec{S}_{45} = [(1,1)]/\sqrt{2}$$
$$\vec{S}_{135} = [(1,-1)]/\sqrt{2}$$
$$\vec{S}_r = [(1,i)]/\sqrt{2}$$
$$\vec{S}_l = [(1,-i)]/\sqrt{2}$$

$$S_0 = I_h + I_v$$
$$S_1 = I_h - I_v$$
$$S_2 = I_{45} - I_{135}$$
$$S_3 = I_r - I_l$$
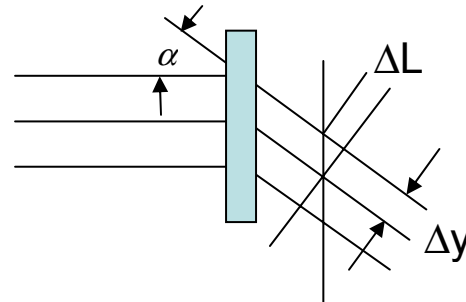
TIME DEPENDENT SIMULATIONS

Figure 4: Pulse lengthening at a transmission grating.

The short time structure of the HGHG FEL-radiation can be spoiled within a beamline. Optical aberrations can cause path length differences. The effects are, however, of minor importance for low divergent FEL-beams. The influence of a grating can be significant. In geometrical optics the path length difference $\Delta L(\Delta y)$ (figure 4) causes

a pulse lengthening of $\Delta T = N\lambda/c$ where N is the number of illuminated lines and c is the velocity of light. In physical optics the wavefront experiences a phase variation of $\Delta\Phi = f(\Delta y)$ where Δy characterizes the displacement in the dispersion direction:

$$\vec{E}(\nu, \Delta y) = \vec{E}_0(\nu, \Delta y) \cdot e^{i \cdot \Delta\Phi}$$
$$= \vec{E}_0 \cdot e^{i \cdot 2\pi\nu \cdot a} \quad (14)$$
$$a = \tan(\alpha) \cdot \Delta y / c$$

The Fourier transformation of this product is the convolution of the time dependent field distribution with a δ-function (eq.15) which is equivalent to the result in geometrical optics.

$$\vec{E}(t, \Delta y) = FFT^{-1}(\vec{E}(\nu, \Delta y))$$
$$= \vec{E}_0(t, \Delta y) \otimes \delta(t - a(\Delta y)) \quad (15)$$

Monochromatic waves are infinitely long. To simulate time dependent effects the simulations have to be extended to a set of frequencies. Assuming only minor phase variations within the FEL-pulse the radiation can be approximated by eq.16.

$$\vec{E}(z, y, t) = \vec{E}_0(z, y) \cdot g(t) \quad (16)$$

The electric field distribution $E_0(z,y)$ is extracted from a time independent FEL-simulation and g(t) has a rectangular (or smoothed rectangular) shape to simulate the time structure. This approximation might be justified for idealized HGHG radiation which is longitudinally fully coherent.

For detailed simulations, however, a set of electric field distributions at various locations within the electron bunch has to be used. The number of slices depends on the time structure and the phase variation within the bunch. Obviously, many more slices are needed for a SASE case as compared to a HGHG case (see figure 5a-b).
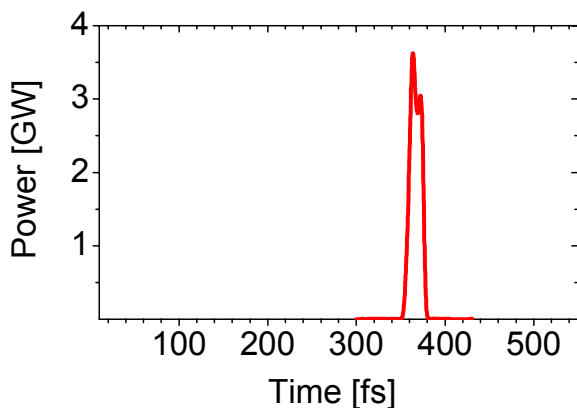

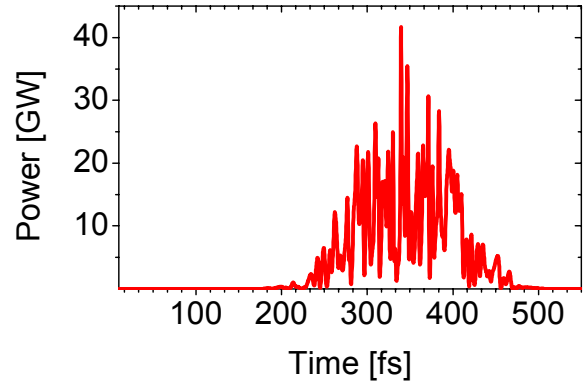Figure 5a: Time structure of the HGHG based BESSY LE-FEL.

Figure 5b: Time structure of a SASE FEL.

The simulation procedure is similar to the one for normal incidence optics. A Fourier transformation of the time dependent data provides the frequency distributions. Each frequency slice is propagated using a physical optics code. The results are Fourier back transformed providing the time structure behind the beamline.

THE PHYSICAL OPTICS CODE PHASE

The equations discussed above have been implemented into the code PHASE. The code is written partly in FORTRAN and partly in C. The power series expansions have all been evaluated using the algebraic code REDUCE [11] which automatically generates FORTRAN code. The graphics are realized with the PAW package of the CERN library. The mouse driven user interface is based on the Motif library. The code runs on a LINUX platform.

After the geometries and optical elements have been defined the parameters are checked and optimized in the fast running ray tracing mode (geometrical optic). Slope errors as well as misalignments of the optical elements can be taken into account. The code provides the possibility to automatically minimize any linear combination of matrix elements of the transformation map (optical aberrations) by variation of defined geometry or mirror parameters. Once, the beamline parameters are fixed, one switches to the physical optics mode and performs the propagation for the defined parameter set.

The representation of the source is a key issue in order to keep the CPU time low. A typical electric field distribution (real and imaginary part) for the spontaneous radiation of an undulator is given in figure 6, top.

The fast oscillating quantities require a fine mesh for integration. The fields can be converted to amplitudes and phases. The discontinuities of the phase distribution can be removed by an appropriate addition of multiples of 2π (figure 6, bottom). In this representation the mesh size can be larger which significantly reduces the CPU time.

Even with optimized integration parameters a time dependent simulation run typically takes several hours on

a single CPU machine. For the simulation of a SASE FEL it will be necessary to run the code on a multi CPU LINUX cluster. The code is suitable for being parallelized since each frequency is independently simulated.
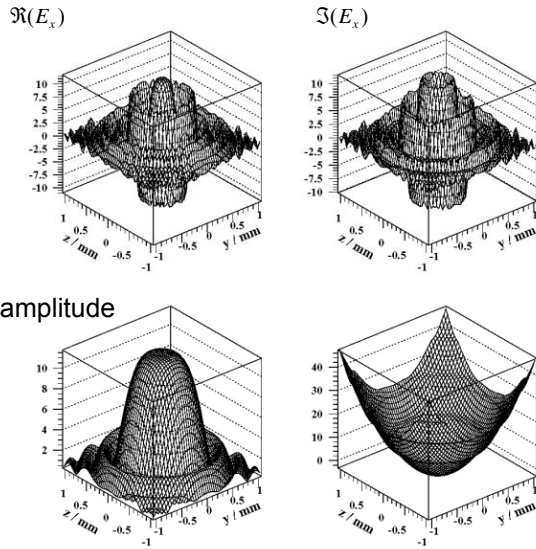

$\Re(E_x)$ $\Im(E_x)$

amplitude

Figure 6: Electric field distribution of a spontaneous undulator source (top) and an equivalent amplitude and phase representation of the same source (bottom).

EXAMPLES

Time Dependent Calculations

The proposed BESSY HGHG based Soft X-Ray FEL facility consists of three independent FEL lines covering the energy regime from 24eV up to 1keV. The FELs are seeded with a Ti:Sapphire laser which determines the pulse length of about 30fs. In case of the high energy FEL the laser wavelength has to be up-converted by a factor of 225 within 4 HGHG stages. The signal to noise ratio decreases quadratically with the harmonic number. A seeding monochromator behind the first stage can significantly improve the photon beam quality [12-13]. The seeding monochromator cleans the spectrum transmitting only the central frequency with a nearly Fourier limited bandwidth without lengthening the pulse duration.

At 24eV a conventional monochromator with one grating would introduce an unacceptable pulse prolongation. Therefore, a dispersion-less double monochromator with a so called 4f-design [12,14] has been proposed. The monochromator consists of two parts which are symmetrically arranged (figure 7). The pulse prolongation of the first grating is compensated with the second grating which operates in opposite order as compared to the first grating. The frequency is selected by simultaneously rotating both gratings. The bandwidth is controlled via the intermediate slit.

In the following we will demonstrate the wavefront propagation method for this seeding monochromator operating at an energy of 24eV.
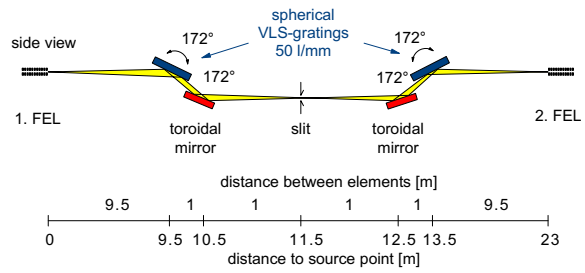

Figure 7: Layout of the seeding monochromator for the BESSY high energy FEL. The monochromator is located behind the first HGHG stage.

For a realistic representation of the longitudinal and transverse properties 840 time slices with a separation of one optical wavelength have been generated with GENESIS. These data have been Fourier transformed. For the PHASE simulations it was sufficient to track only 40 frequencies (figure 8) because the variations over the pulse length are only moderate. For a SASE field it is expected that the number of frequencies is about two orders of magnitude larger.
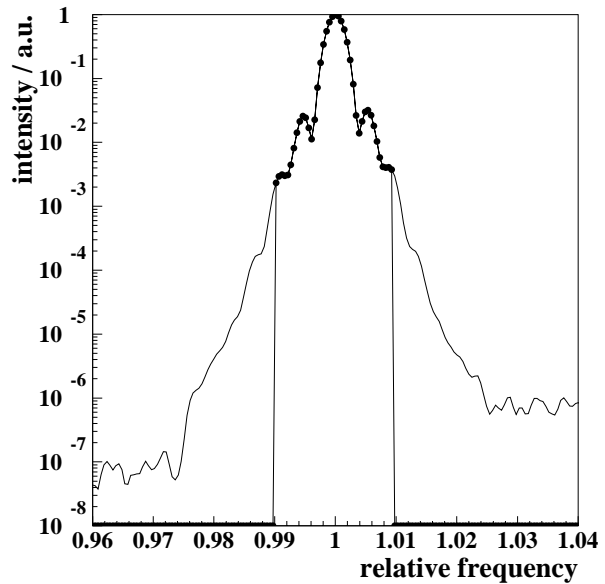

Figure 8: Spectral distribution of the input pulse. The frequencies used for the simulations are marked.

Figure 9 demonstrates a significant pulse lengthening behind the first two elements of the monochromator. For comparison the results for a toroidal mirror with a strong demagnification are plotted (184° total deflection angle, r=20000mm, r'=1000mm). The time structure is not significantly affected in this case which is due to the small divergence of the beam.

For an open intermediate slit the spectral width is identical to the width at the exit of the first FEL stage (figure 10). A reduction of the slit height to 20μm reduces the spectral width by a factor of three.
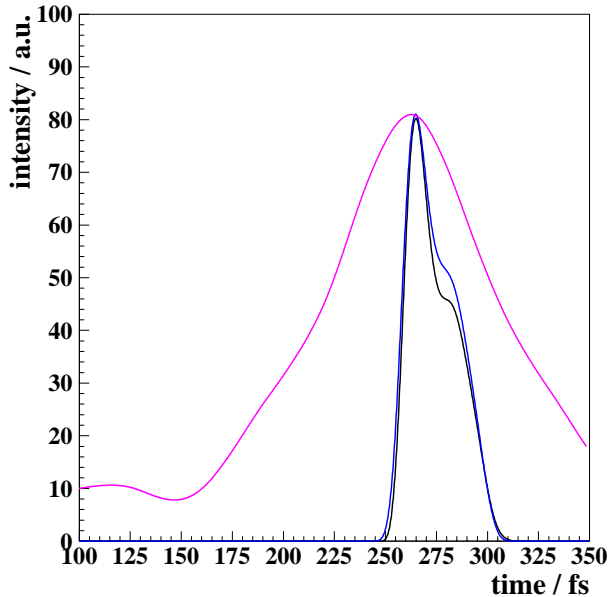

Figure 9: Time structure of the FEL-pulse at the exit of the final amplifier (black) and at the intermediate slit of the seeding monochromator (magenta). For comparison the time structure behind a toroidal mirror with a demagnification of 20:1 is plotted as well (blue).
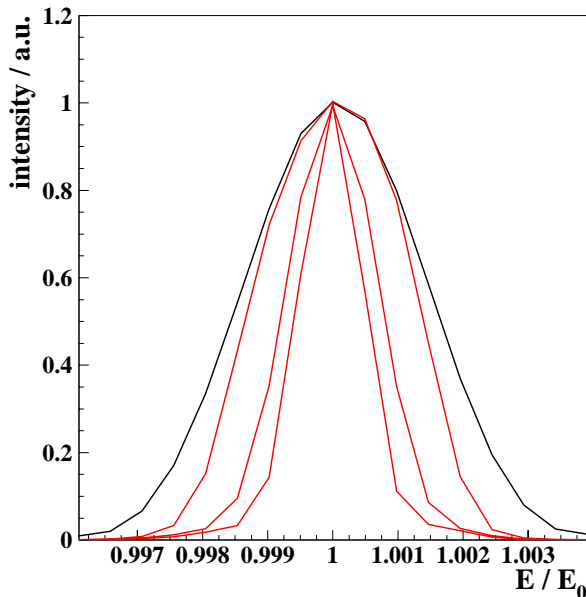

Figure 10: Spectral width at the intermediate slit for slit open (black) and slit closed to 100, 50 and 20μm (red).

As demonstrated in figure 11 the time structure at the symmetry point of the monochromator depends on the vertical position (dispersion direction). To a certain extent

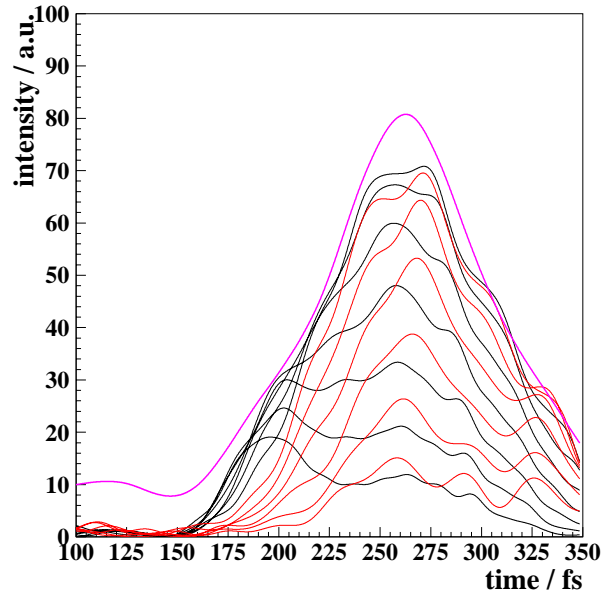this provides a knob for coherent control using specially formed slit plates.

Figure 11: Time structure at the intermediate slit plane (figure 7) at various vertical positions (black: below, red: above midplane) and the sum of all contributions (magenta, this intensity not to scale).
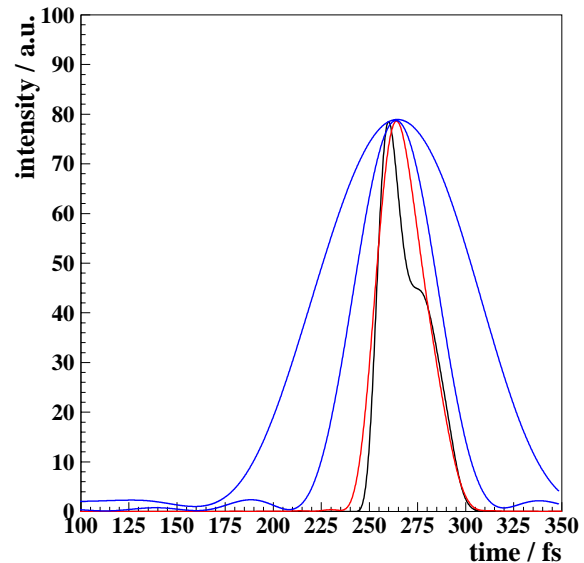

Figure 12: Time structure of the original pulse (black), the pulse at the monochromator exit with intermediate slit at 300μm (red) and closed to 100 and 50μm (blue).

In a second step the complex electric field distribution at the intermediate slit has been used as a source for the propagation across the second half of the monochromator. With the central slit set to 300μm the original pulse width is nearly recovered (figure 12). The differences between the two curves can be explained by the diffraction at the

slit and by the limited width of the time window which has been used. The intensity does not drop to zero in figure 9 which gives rise to numerical noise. Closing the central slit the divergence of the radiation gets larger due to diffraction. The number of illuminated lines increases and, hence, the pulse is getting longer (figure 12).

In [12] it is pointed out that a slit height of 300μm enhances the output power and reduces the bandwidth at the end of the complete FEL significantly. The influence of smaller slit sizes which must not scrape the Fourier limited part will be subject to further studies.

Following the described procedure the properties of the monochromators behind the final amplifiers of the three BESSY FEL lines will be studied in the future. Another monochromator in 4f geometry is planned behind the final amplifier of the low energy FEL [4]. Due to the smaller wavelengths the monochromators for the medium and high energy FEL provide the possibility to control the pulse length and bandwidth by adjusting the angle of incidence at the grating and thus the number of illuminated lines [4].

Polarization Effect

Many experiments benefit from the variable polarization of the synchrotron radiation. Modern insertion devices (e.g. of APPLE type) provide any arbitrary state of polarization. The user is interested in the polarization properties at the sample. Therefore, the polarization properties have to be transformed correctly through the beamline.

The state and degree of polarization is not constant but may change throughout the beamline. This will be demonstrated for the example of a double undulator. Double undulators are needed for fast helicity switching. One undulator provides right handed and the other one left handed circularly polarized light. A fast chopper downstream of the beamline or alternatively, an aperture in combination with a periodic displacement of the electron beam separates the two light cones with high frequencies. Double undulators are installed at various third generation storage rings (ESRF, BESSY, SLS, SPRING8 [15-18]). At the SLS the undulator segments are transversally displaced. The principle layout is plotted in figure 13.
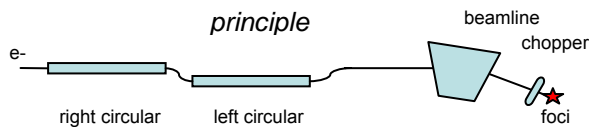
Figure 13: Layout of the SLS double undulator.

Figure 14 shows the parameters S2 and S3 in the focal plane. The two light cones are well separated and can be chopped. Out of focus (figure 15) the two light cones are smeared and a significant S2 component shows up. Such simulations are useful to determine the optimum position of the chopper.
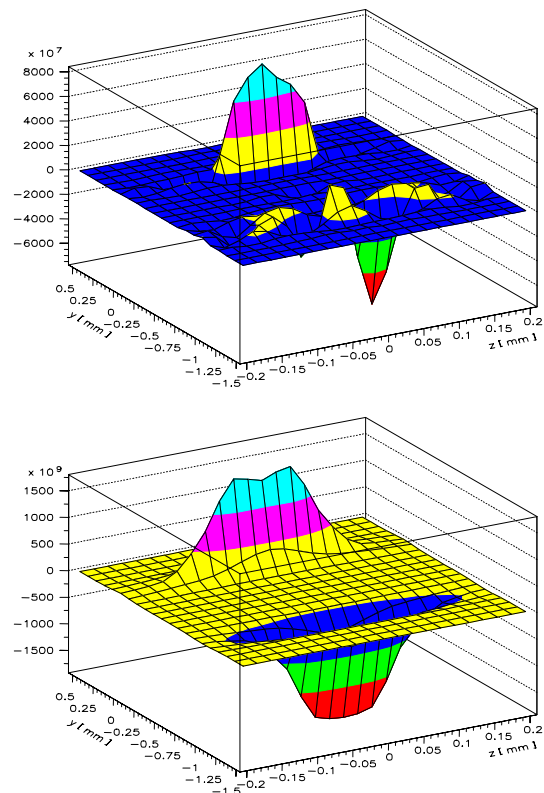
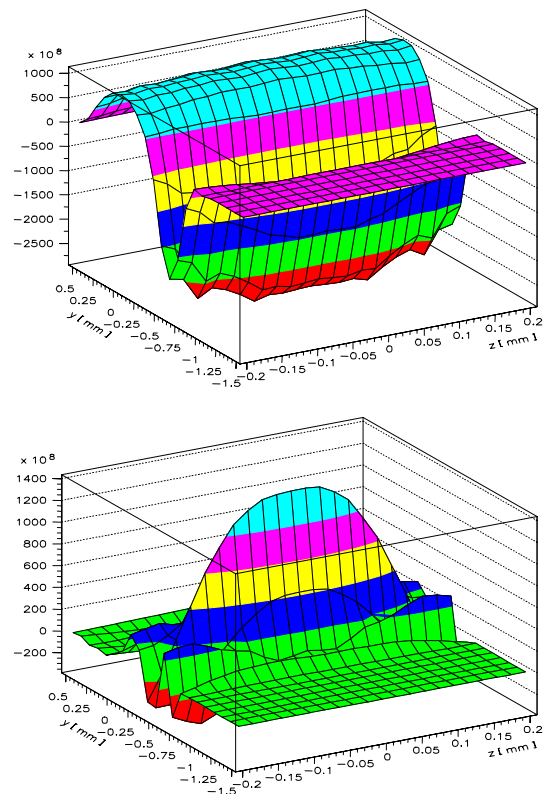Figure 14: S2 (top) and S3 (bottom) component of the double undulator radiation at the focal point.

Figure 15: S2 (top) and S3 (bottom) component of the double undulator radiation upstream of the focal point.

CONCLUSION

The radiation properties of the new soft X-ray and X-ray FEL facilities are quite different compared to third generation light sources. The simulation of short pulses as well as transverse and longitudinal coherence requires new techniques which go beyond the features of conventional ray tracing codes. We presented a general approach based on physical optics which is appropriate to simulate the FEL properties. Realistic transverse and longitudinal pulse characteristics can be taken into account. Using the described procedures the dependence of the pulse length and the spectral width of a seeding monochromator have been studied. In a second example the polarization properties within a beamline behind a double undulator for fast helicity switching has been simulated. The technique implemented into the code PHASE is already well suited to cope with the specific radiation properties of HGHG FELs. For SASE FELs the code has to be adapted to a multi CPU cluster to keep the computation time within reasonable limits.

REFERENCES

[1] TESLA-Technical Design Report, TESLA X-FEL, Technical Design Report, 2002-9, 2002.

[2] Linac Coherent Light Source (LCLS), Conceptual Design Report, SLAC-R-593, 2002.

[3] T. Shintake, Nucl. Instr. and Meth., A507 (2003) 382-397.

[4] The BESSY Soft X-ray Free Electron Laser, Technical Design Report March 2004, eds.: D. Krämer, E. Jaeschke, W. Eberhardt, ISBN 3-9809534-08, BESSY, Berlin (2004).

[5] J. W. Goodman, "Introduction to Fourier Optics", McGraw-Hill Physical and Quantum Electronics Series, New York, 1968.

[6] S. Reiche, GENESIS 1.3, Nucl. Instr. Meth. A 429 (1999) 243.

[7] Meseck et al., these proceedings.

[8] J. Bahrdt, Applied Optics, 34 (1995) 114-127.

[9] J. Bahrdt, Applied Optics, 36 (1997) 4367-4381.

[10] L. Mandel, E. Wolf, "Optical Coherence and Quantum Optics", Cambridge University Press, 1995.

[11] A. C. Hearn, "REDUCE 3.5, A General Purpose Algebra System" [RAND, Santa Monica, Calif. 90407-2138 (reduce@rand.org), 1993].

[12] M. Abo-Bakr et al., these proceedings.

[13] K. Goldammer, M. Abo-Bakr, R. Follath, A. Meseck, these proceedings.

[14] D. Goswami, Phys. Rep. 374/6 (2003) 385;

[15] P. Elleaume, J. Synchr. Rad. 1(1994) 19-26; P. Elleaume, Nucl. Instr. and Meth., A304 (1992) 719-724.

[16] J. Bahrdt et al., Nucl. Instr. and Meth., A467-468 (2001) 21-29.

[17] C. Quitman et al., Surface Science, 480 (2001) 173-179.

[18] T. Hara et al., J. Synchr. Rad., 5 (1998) 426-427; T. Hara et al., Nucl. Instr. and Meth., A498 (2003) 496-502.